SUPPLEMENTARY INFORMATION

High-Contrast Imaging of Nanodiamonds in Cells by Energy Filtered and Correlative Light-Electron Microscopy: Toward A Quantitative Nanoparticle-Cell Analysis

Shen Han,[‡, 1] Marco Raabe,[‡, 1, 2] Lorna Hodgson,[3] Judith Mantell,[3] Paul Verkade,[3] Theo Lasser,[1,4] Katharina Landfester,[1] Tanja Weil,[*, 1, 2] Ingo Lieberwirth,[*, 1]

Material. Fluorescent nanodiamonds (fND) were bought from FND Biotech (Taiwan).

Synthesis of dcHSA-PEG. The cationization, denaturation and the attachment of polyethylene glycol of human serum albumin (HSA) was synthesized as reported before.[1] In summary, HSA was converted to cationic HSA (cHSA) by adding ethylenediamine in high access resulting in ≈158 positive charges per protein. The positive surface charge enables high uptake into human cancer cells due to interactions with the negative charged cell membrane. Afterwards, in average 18 PEG chains (MW = 2000 g/mol) were attached to the cHSA. The PEG chains are necessary to enable colloidal stability, reduce interaction with plasma proteins and prevent immunoresponse. The obtained cHSA-PEG$(2000)_{18}$ was denatured using an urea buffer (phosphate buffer 50 mM, pH 7.4, 5 M urea, 200 mM ethylenediaminetetraacetic acid) and the disulfide bridges were reduced by tris(2-carboxyethyl)phosphine (TCEP). N-(2-aminoethyl)maleimide trifluoroacetic acid salt was added to cap the free thiol groups to prevent rebinding and to form the final dcHSA-PEG$(2000)_{18}$.

Characterization of coated fNDs. The successful coating of fNDs can be controlled by dynamic light scattering (DLS), zeta-potential and transmission electron microscopy (TEM) measurements. Usually, uncoated fNDs aggregate strongly in aqueous buffer solutions; however, in MilliQ water DLS of fNDs can be measured without aggregation. The DLS measurements showed an increase of R_h from 44.5 nm to 61.7 nm (Figure S2-3) after coating the fNDs with dcHSA-PEG$(2000)_{18}$. One of

the reasons of the relatively large increase in R_h (17.2 nm) is the loss of small fND during the purification by centrifugation. Furthermore, the coated fNDs showed only one population in the DLS measurement recorded at different angles indicating the presence of only single fNDs (Figure S2-3). The surface of these commercial available fNDs is oxidized and therefore, the fND possess a negative surface charge (Figure S1d). Due to the negative charge and the strong aggregation in aqueous buffer, uncoated fNDs were not taken up into human mammalian cancer cells. After the adsorption of dcHSA-PEG onto the fNDs, the surface charge changed from a negative to positive value (Figure S1d) caused by the positive charge of the dcHSA-PEG$(2000)_{18}$. The coated fNDs showed strong uptake into human mammalian cancer cells even at low concentrations.

fNDs can be easily visualized by TEM due to their high density. Uncoated fNDs showed mostly aggregation in DPBS on the TEM grid (Figure S1a). In contrast, coated fNDs in DPBS were nicely distributed over the TEM grid (Figure S1b). Monodispersed coated fNDs in DPBS are highly important for further in vitro studies.

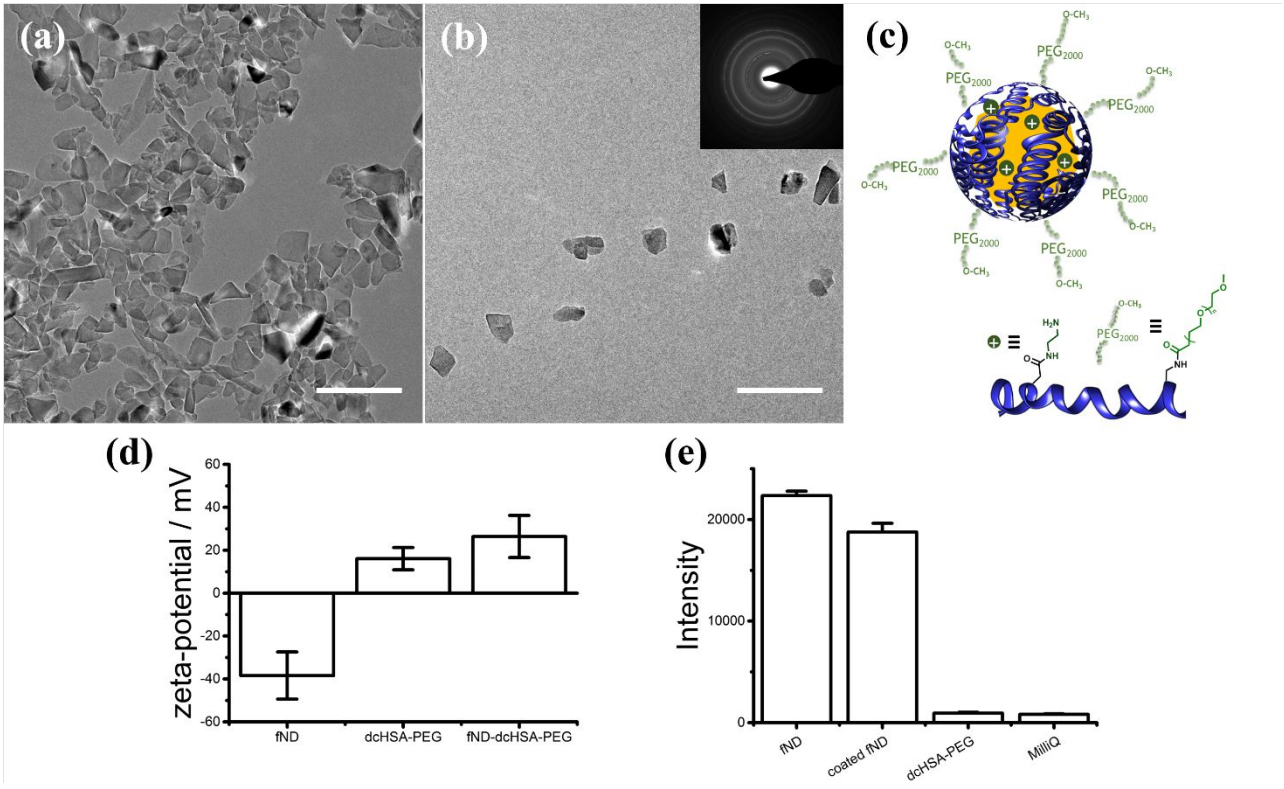

Figure S1: Characterization of fND. (a) Transmission electron microscopy (TEM) images of uncoated fND aggregates diluted in PBS. (b) Coated single fNDs diluted in PBS; fresnel

diffraction pattern of ND. (c) Scheme of protein coated fNDs. (d) Zeta-potential values. (e) Fluorescence intensity of uncoated fNDs, coated fNDs (both 0.5 mg/ml), dcHSA-PEG (2 mg/ml) and MilliQ water. Scale bar: 200 nm.

Coating of NDs. 500 µg of fluorescent NDs were dispersed in 5 ml of MilliQ water. Afterwards, the solution was dropped into a mixture of 2 mg dcHSA-PEG in 20 ml MilliQ water and shaken overnight at room temperature. The next day, free protein was removed by centrifugation (18 000 g, three times with MilliQ).

For further *in vitro* experiments, the fNDs were dispersed in Dulbecco's Phosphate Buffered Saline at a concentration of 1 mg/ml.

Fluorescence measurement. Fluorescence was measured using Tecan (SPARK 20M). Uncoated and dcHSA-PEG coated fNDs were dispersed in MilliQ water at a concentration of 0.5 mg/ml. dcHSA-PEG was dissolved in MilliQ water at a concentration of 2 mg/ml. 10 µl of each sample were transferred into a 96-well plate and the emission at a wavelength of 680 nm was measured at a fixed gain of 167. The excitation wavelength was 561 nm.

DLS. Dynamic light scattering measurements were performed on an ALV spectrometer consisting of a goniometer and an ALV-5004 multiple-tau full-digital correlator (320 channels). A He-Ne Laser (wavelength of 632.8 nm) was used as light source. For temperature controlled measurements, the light scattering instrument was equipped with a thermostat from Julabo. Measurements were performed at 20 °C at 9 angles ranging from 30° to 150°. The full measurements are depicted in Figure S2-3 left. The autocorrelation curve of the measurements at 90° is shown in Figure S2-3 right. The autocorrelation curve was transferred into a time based function to visualize the monodispersity of the samples using the software contin algorithm (Figure S2-3 right blue).

Uncoated and dcHSA-PEG coated fND were prepared at a concentration of 0.5 mg/ml in MilliQ water for DLS measurements.

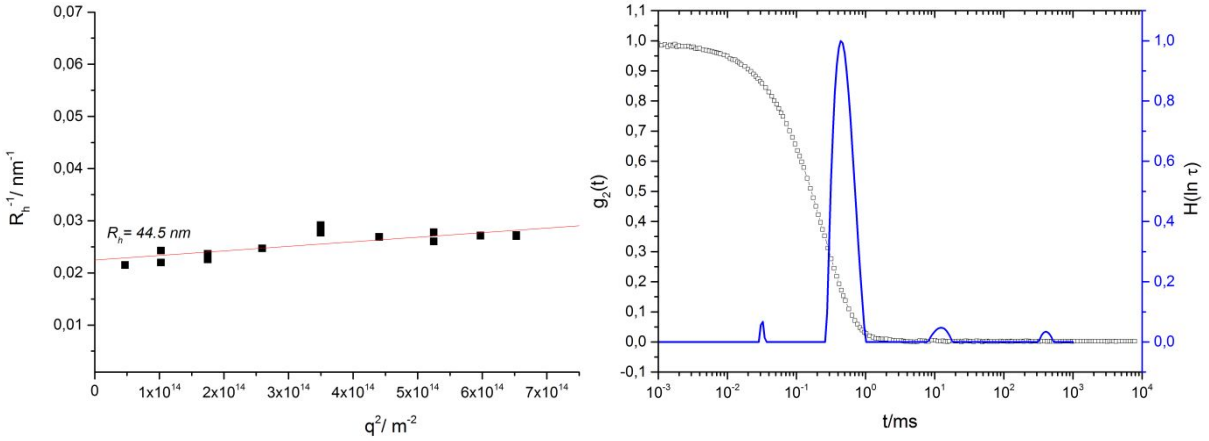

Figure S2: DLS of uncoated fNDs. Left DLS measurements from 30° to 150°. Right Autocorrelation curve (black dotted line) and time based function (blue) at 90°.

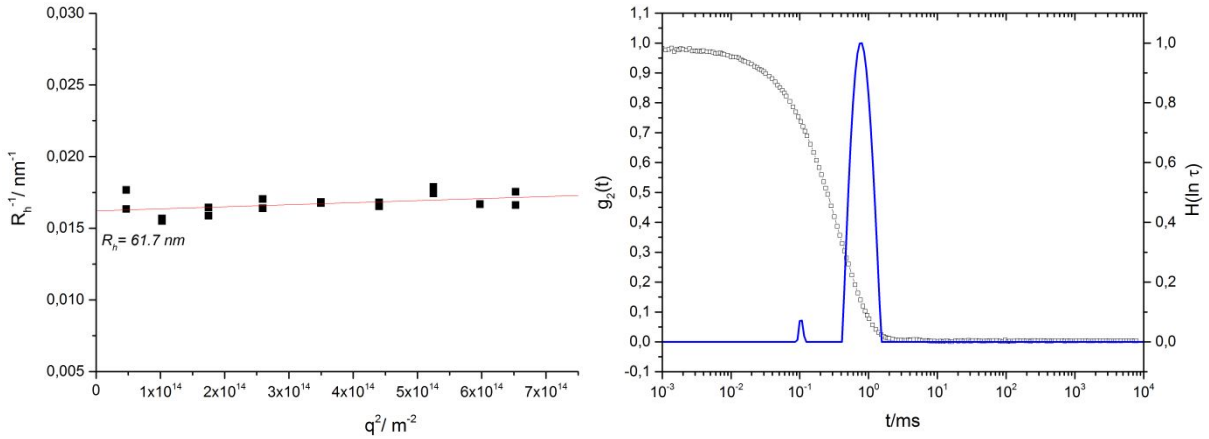

Figure S3: DLS of fNDs coated with dcHSA-PEG. Left DLS measurements from 30° to 150°. Right Autocorrelation curve (black dotted line) and time based function (blue) at 90°.

Zeta-Potential. Uncoated (0.5 mg/ml), dcHSA-PEG coated fND (0.5 mg/ml) and dcHSA-PEG (0.5 mg/ml) were prepared in a 1 mM KCl solution and the zeta-potential was measured using a Zetasizer (Nano series) from Malvern.

Cell culture. HeLa cells were cultured in Dulbecco's modified eagle medium (DMEM; Invitrogen, Germany) supplement with 10% fetal bovine serum (FBS; Sigma Aldrich, Germany), 1% glutamine, and 1% penicillin/streptomycin (Invitrogen, Germany) in a humidified incubator at 37 °C and 5%

CO_2.

Preparation of in-dish correlative light-electron microscopy (CLEM) specimens for confocal light scanning microscopy (CLSM) and transmission electron microscopy (TEM). In-dish CLEM was defined as the detection of fluorescence signals prior to EM preparation. HeLa cells were incubated with fNDs (75 μg/ml) at 37 °C (5% CO_2) for 4 h and then fixed in 4% formaldehyde (Carl Roth, Germany) for 10 min in MatTek gridded glass bottom dishes (Ashland, USA). Nucleus counterstaining with Hoechst 33342 dye in DMEM (1:1000) was performed after the paraformaldehyde (PFA) fixation for 5 min. Three times of washing in PBS were performed after nucleus staining. Prepared samples were investigated on Leica SP8 AOBS system attached to a Leica DM I6000 inverted microscope with a 63X 1.4 NA oil immersion objective. The Hoechst 33342 dye and fNDs were excited with 50 mW diode laser at 405 nm and 20 mW solid state yellow laser at 561 nm. Fluorescence signals were collected at 461 nm for Hoechst and 660-700 nm for fNDs. Stack images of ROIs with the step of ~0.2 μm were recorded. The position of the cell of interest was simultaneously recorded. After fluorescent imaging, samples were subjected to a postfixation in 4% glutaraldhyde in phosphate buffer (pH = 7). Staining with OsO_4 and uranyl acetate were performed sequentially, each step followed by three times washing in phosphate buffer. Samples were then subjected to dehydration through ethanol in ddH_2O with the gradient of 70%, 80%, 90%, 100% for 10 min each and subsequently embedded in EPON. Polymerized blocks were trimmed to the ROIs recorded by CLSM, and cut into 300 nm thick sections using a 45º diamond knife (Diatome, Switzerland) in EM UC6 ultramicrotome (Leica, Germany). Sections were then collected onto formvar coated slot copper grid (Plano, Germany) and air dried overnight for TEM imaging and tomography. Region of interests (ROIs) were retraced in TEM and tomography was performed with a single-axis tilt series from -65.5° to +67° using tilt increments of 1.5º above +/- 45° and 2.5º between -45° and +45°. Totally 65 images were collected using a CCD Camera. TEM imaging and

tomography were performed with a Tecnai G20 - FEI 200 kV Twin Lens with Lab6 filament and FEI Eagle 4k x 4k CCD camera and with a Tecnai F20 – FEI 200 kV with FEG and Gatan US1000 CCD camera.

Preparation of in-resin CLEM specimens for CLSM and TEM. In-resin CLEM requires samples to be vitrified and embedded into resin prior LM and EM acquisition. HeLa cells were incubated with fNDs (75 µg/ml) for 4 h at 37 °C (5% CO_2). After the cell uptake experiment, cells in the petri dish were harvested and transferred into 2 ml Eppendorf tubes. After centrifugation at 1000 g for 5 min, 1 µl of thick cell suspension were collected and loaded into a 100 µm deep membrane carrier (Leica, Germany) and vitrified in Leica EM PACT2 (Leica, Germany). Frozen membrane carriers were then transferred into flow through containers with freeze substitution cocktail (0.1% uranyl acetate, 0.01% tannic acid, 5% water in acetone). Freeze substitution was done in an AFS2 automated freeze substitution device (Leica, Germany) equipped with an attachment for automated exchange of reagent (Freeze substitution processor, FSP, Leica, Germany). Samples were kept at -90 °C for 5 h and gradually warmed up to -45 °C at the rate of 5°C/h. After being held at -45 °C for 2 h, samples were washed twice in acetone for 30 min each. Samples were then infiltrated in 25%, 50%, 75% of Lowicryl HM20 resin in acetone for 2.5 h each and finally infiltrated in 100% resin overnight. Resin was exchanged for twice with the duration of 3 h each after the overnight infiltration. Polymerization of resin was carried out under UV light for 43 h, with the first 19 h being held at -45 ℃, followed by warming up to 0 ℃ within 12 h, and finally being kept at 0 °C for another 12 h.

After polymerization, resin blocks were removed from the containers. The carriers were detached from the resin blocks by using liquid nitrogen and the warmed up specimen carrier detaching tool (Leica, Germany). The blocks were then trimmed to desired sizes and sectioned to 120 nm thick sections using a 45º diamond knife (Diatome, Switzerland) in EM UC6 ultramicrotome (Leica,

Germany). Sections were collected onto carbon coated formvar films on F1 copper finder grids (Agar Scientific). After being air dried, grids were stained with Hoechst 33342 dye in ddH_2O (1:1000) for 5 min, and washed three times in ddH_2O for 1 min each. Each stained grid was then mounted between a coverslip and a glass slide in 15 µl of 50% glycerol in ddH_2O. Mounted grids were then imaged by Leica DMI4000 B inverted epifluorescence microscope with 20X 0.75 NA dry lens for fluorescence detection. After imaging, the grids were carefully retrieved using a sharp razor blade and washed in H_2O. The grids were then post-stained with uranyl acetate and lead citrate before TEM imaging.

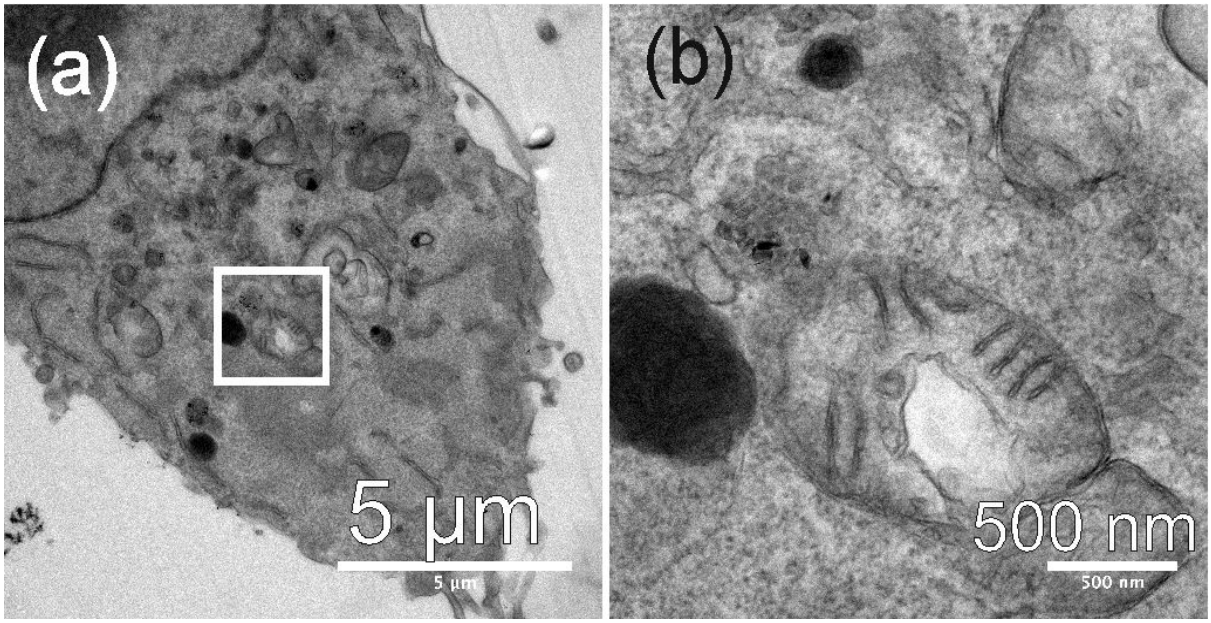

Figure S4: TEM bright field (BF) micrographs showing the preservation quality of the in-dish preparation method.

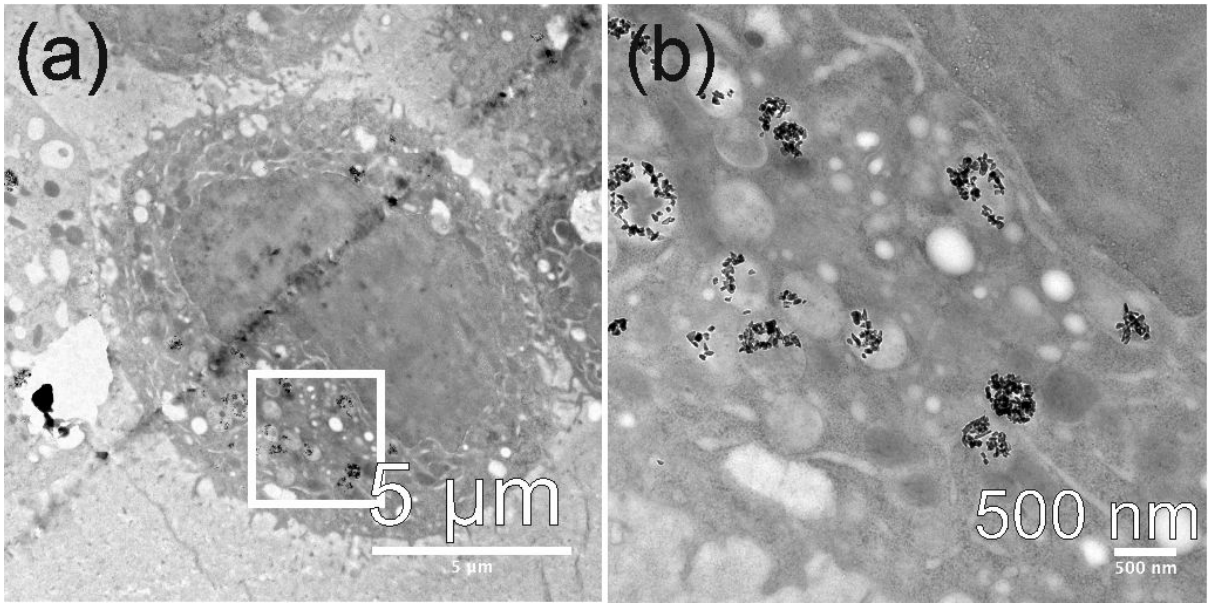

Figure S5: TEM BF micrographs showing the preservation quality of the in-resin preparation. Compared to the in-dish method, the contrast of the cellular structures is lower, presumably due to the missing OsO_4 staining and lower uranyl acetate concentration. However, post staining of the sections should be possible.

Images alignment and analysis. For tomogram alignment and reconstruction, IMOD software (version 4.9.7) was used. Acquired images from the tilt series were initially aligned and stacked in the software. The stacked file was then computationally reconstructed using a weighted back-projection algorithm. For CLEM image registration, images from light and electron microscopy were manually tracked and aligned using eC-CLEM plugin in Icy.[2]

The alignment of the in-resin acquired data was straightforward, because both, electron and light microscopical imaging originate from the very same specimen. However, for the in-dish preparation, there is a certain time span between the LM imaging and the final fixation for EM preparation and subsequent imaging. This time span already leads to systematic mismatch in the alignment. In addition, the preparation of the ultrathin sections might lead to problems with the CLEM alignment. The sections suffer a certain compression during sectioning, which can be easily compensated by a simple affine transformation (stretching of the EM micrographs parallel to the cutting direction). However, we did not observe noticeable compression of the sections and within the accuracy of the

LM images we did not need to compensate for this. On the other hand, the normal of the sections and the optical axis of the LM might not coincide. With other words, there is a certain angle between the cutting direction and the imaging direction of the LM. For this case, there is a certain tolerance of the preparation method due to the rather large confocal optical section thickness compared to ultramicrotomy sections. A confocal microscope can reach thicknesses down to 500 nm. The effect of a misaligned cutting angle would result in the disappearance of (correlative) objects, especially at the image periphery. Accordingly, we put much effort in aligning the block phase of the resin block as parallel as possible to the diamond knife and we did not encounter any problems with a misalignment of the cutting angle with regards to the imaging plane of the LM.

Transmission electron microscopy. TEM examination was performed on a Tecnai F20 transmission electron microscope operated at an acceleration voltage of 200 kV. The instrument was equipped with a scanning unit for scanning TEM (STEM) and a Tridiem 863 (Gatan) post column electron energy loss spectrometer capable of both, electron energy loss spectroscopy (EELS) and image filtering (EFTEM). Conventional image acquisition was done with a Gatan US 1000 CCD Camera at on-axis position. In post-filter position another Gatan US1000 CCD camera was used for EFTEM and EELS. For bright field imaging and for the acquisition of tomogram tilt series an objective aperture with diameter of 20 µm was used. The same aperture was used for dark field imaging; the beam tilt was adjusted to a value around 2 x 6.1 mrad, which is the angle of the diamond (111) diffraction for 200 kV electrons. Under these conditions, only electrons that have been diffracted (or inelastically scattered) exactly to the hole of the objective aperture contribute to the image formation. With this imaging mode it is possible, to identify and highlight crystalline areas in the specimen.

STEM was done using a fishione high-angle annual dark-field (HAADF) detector and if not otherwise stated, the camera length was adjusted to 520 mm. At this camera length the diamond (111) diffraction angle falls into the acceptance angle of the HAADF detector and hence the crystalline areas yield

bright contrast.

EFTEM was done using an energy selecting slit width of 10 eV, if not otherwise stated.

Imaging of NDs in the TEM. Imaging of NDs and especially individual NDs in TEM can be facilitated by using different imaging methods, depending on the configuration of the respective instrument. The main problem when imaging ND in a resin matrix, as commonly prepared for TEM ultrastructural examination of biological samples, is their low contrast with regard to the surrounding resin. However, there are some physical features of NDs that promote their discrimination from the resin matrix. The density of a diamond is with 3.5 g/cm^3 much higher than that of the surrounding resin and, as every diamond, NDs are crystalline.

Imaging crystalline areas is one of the strengths of the TEM. By simply selecting the position of the objective aperture, it is possible to select electrons, that have left the sample under a certain angle, e.g. due to diffraction. This method is called dark field mode and can be easily achieved in any TEM. The strongest diffraction spot of diamond is the (111) with a *d*-spacing of 2.058 Å. This corresponds to a diffraction angle of $2\Theta = 12.2$ mrad for 200 keV electrons. When the objective aperture of the TEM is adjusted in a way that electrons leaving the sample under this angle can pass (but the transmitted beam is blocked), the crystalline areas appear with bright contrast. But because the aperture allows only a small azimuth area of the diffraction ring to pass, only those crystals with the correct orientation become visible (arrow in Figure S6c).

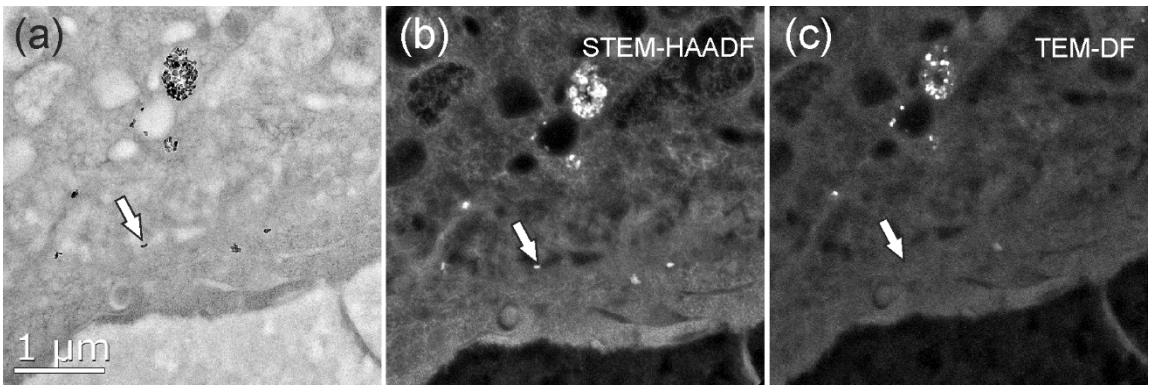

Figure S6: TEM and STEM micrographs showing the same area. In the bright field micrograph (a) the NDs are clearly visible by their dark contrast and in the STEM micrograph (b) the NDs appear bright because their diffraction contributes to the HAADF signal. All the NDs in the bright field micrograph are also visible in the STEM micrograph. When using the conventional TEM dark field (c) mode, some of the NDs are not visible, as exemplarily marked by the arrow.

In order to overcome this azimuthal restriction, annular detection methods like conical dark field or HAADF-STEM can be used. Due to the annular geometry of the HAADF detector all directions of the diffraction ring are detected and the crystal areas appear with bright contrast (Figure S6b). But even using the whole (111) diffraction ring does not guarantee that every ND crystal becomes visible, because this depends on the crystalline orientation; if the Bragg-condition is not fulfilled due to an odd orientation of the crystal there is no signal in the dark field micrograph. This is exemplarily demonstrated in Figure S7, where the ND marked by the arrow is clearly seen in the TEM BF (a) and in the EFTEM micrograph (c), but not in the HAADF-STEM (b).

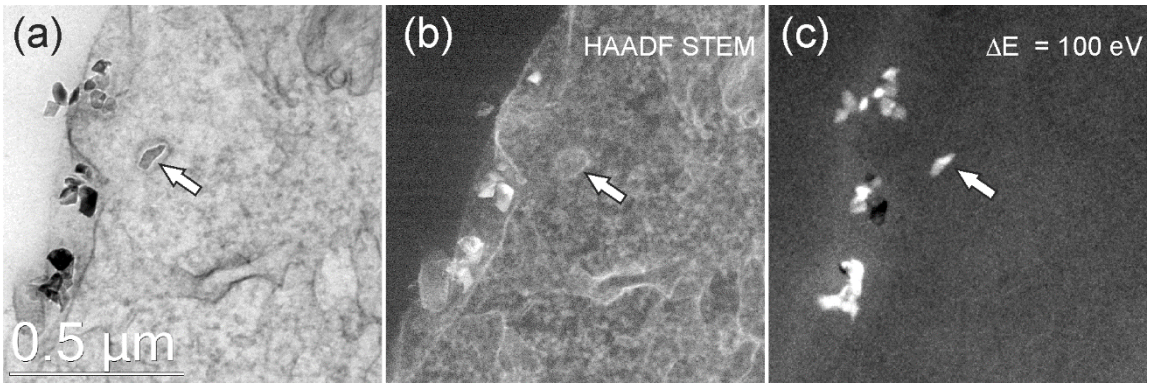

Figure S7: TEM-BF (a), STEM-HAADF (b) and EFTEM (c) micrographs of the same area. The ND marked with an arrow is visible in the BF and the EFTEM micrograph, but it does not appear in the HAADF-STEM mode.

Another alternative to image NDs in a resin matrix is to use EFTEM imaging. Here, the identification does not rely on the correct orientation of the crystal but rather on the difference in electron density between the ND and the surrounding matrix. NDs are a pure carbon material and the surrounding matrix of polymerized resin is a carbon rich material as well. Accordingly, element specific discrimination by EFTEM is eliminated. But the mean free electron path λ depends on the local electron density and then finally on the density of the respective material. In a simplified explanation the probability for inelastic scattering depends on the local electron density and with that on the material density. This is shown in the electron energy loss (EEL) spectra Figure 3g. The intensity in the areas of the nanodiamonds is greater in the entire spectral range measured from 50 to 200 eV than where resin or cellular material is present in the sample. Therefore, the nanodiamonds appear brighter in the EFTEM micrographs. Figure S8 shows an EFTEM series acquired at different energy losses using an energy selecting slit width of 10 eV. The NDs are clearly visible up to 190 eV energy loss. We did not checked higher loss values because this would unnecessarily increase the exposure time without yielding more information. Accordingly, EFTM imaging is the appropriate way to identify and image NDs in an embedded cell samples. Even single fNDs can be detected this way, which is not possible by fluorescence imaging at all.

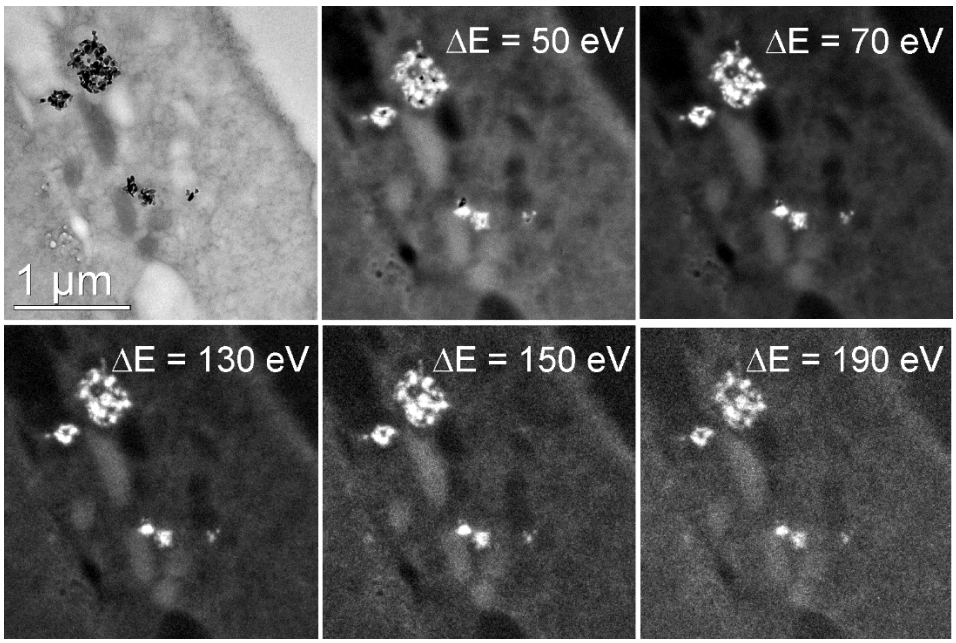

Figure S8: energy filtered TEM micrographs: The sample area is imaged with increasing energy loss from bright field (0 eV, upper left) to 190 eV (lower right). The slit width of the spectrometer was adjusted to 10 eV. In the bright field micrograph the ND are clearly visible by their dark contrast.

However, if you have neither an energy filter nor a scanning unit at the TEM, there is another, very easy way to locate the embedded NDs. Hereby one can simplify the tedious search for the NDs considerably. Like other objects, NDs are phase objects that change the phase of the electron waves as they exit the sample.

If the TEM is now heavily overfocused, this will cause the resulting Fresnel fringes of the NDs to show bright contrast on the resulting image, as shown in Figure 9b. Although these images are useless for further processing, they clearly show the position of the NDs. For comparison, Figure 9c shows the corresponding EFTEM image, on which individual NDs can be recognized as well (marked by the arrow).

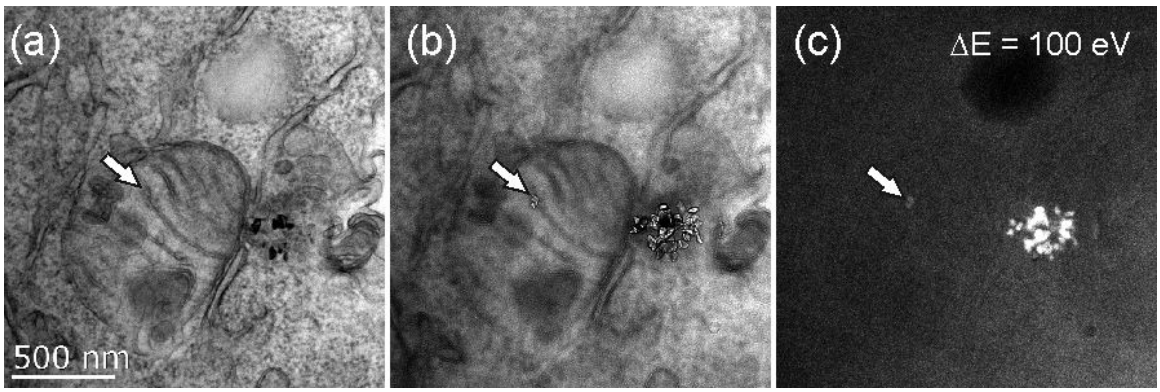

Figure S9: TEM and EFTEM micrographs of the same sample area demonstrating the ease and power of overfocus identification of phase objects like NDs in a resin matrix. (a) The TEM BF micrograph does not reveal the presence of a ND at the position marked with an arrow. Over focused TEM micrograph (b) clearly shows the ND which can be seen in the EFTEM micrograph (c) as well.

Calculation of signal to noise ratio

The signal-to-noise ratio of the gray value depicted in Figure 3b-c was calculated by Gaussian fitting. The two Gaussian fits for the TEM bright field image and the EFTEM image are shown in Figure S10-11.

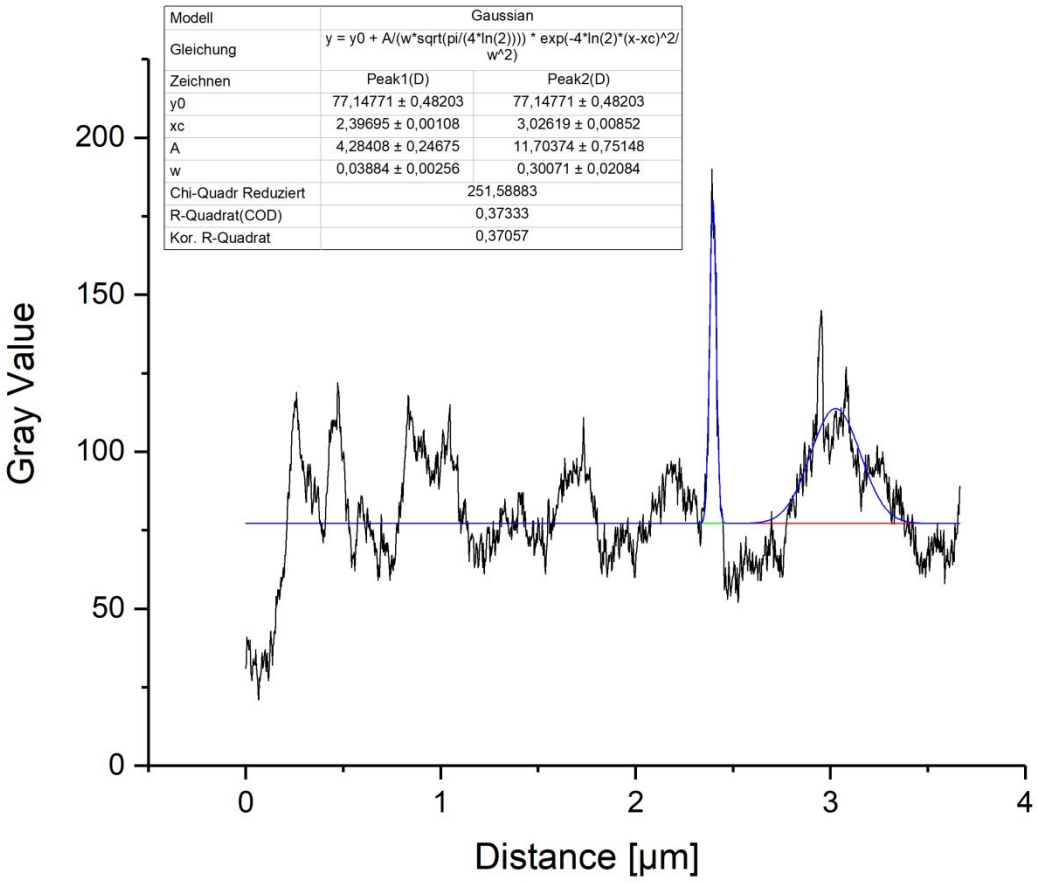

Figure S10 The Gaussian fit of the gray value graph from the TEM bright field image (Figure 3b).

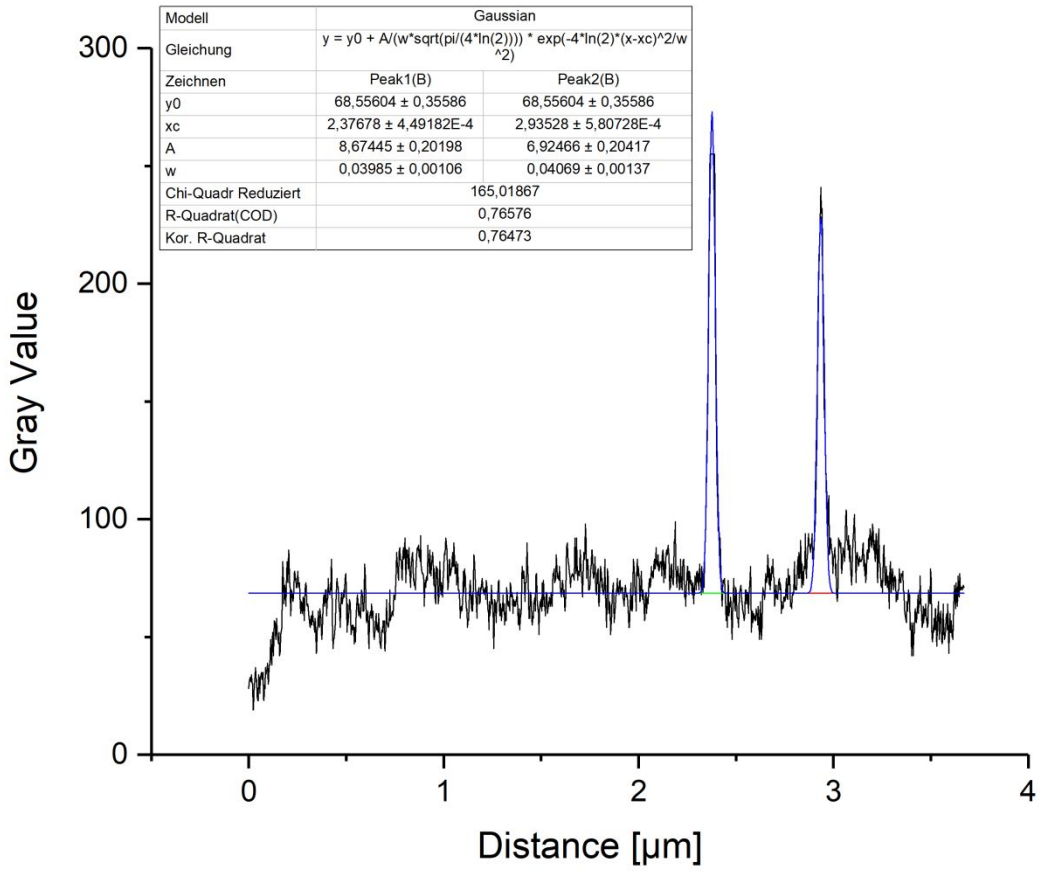

Figure S11 The Gaussian fit of the Gray Value graph from the EFTEM image (Figure 3c).

Calculation of resolution

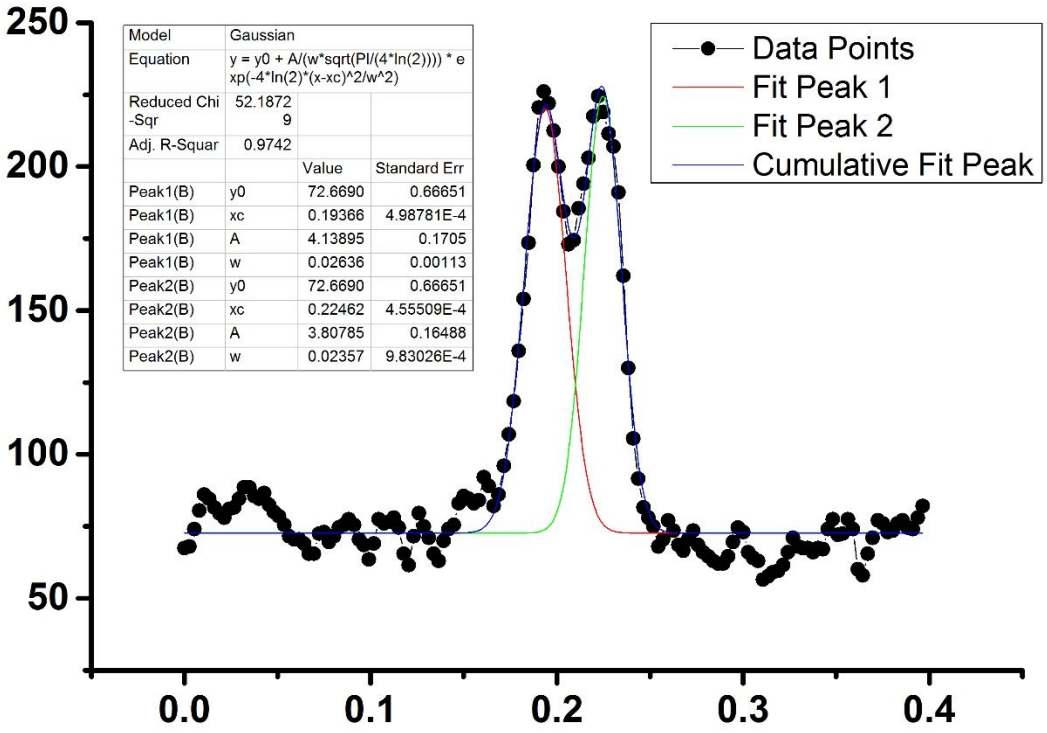

Figure S12 The two peaks were fitted by a Gaussian which was used to calculate the resolution.

References:

1. Wu, Y. Z.; Ermakova, A.; Liu, W. N.; Pramanik, G.; Vu, T. M.; Kurz, A.; McGuinness, L.; Naydenov, B.; Hafner, S.; Reuter, R.; Wrachtrup, J.; Isoya, J.; Fortsch, C.; Barth, H.; Simmet, T.; Jelezko, F.; Weil, T. *Adv. Funct. Mater.* **2015,** 25, (42), 6576-6585.

2. Paul-Gilloteaux, P.; Heiligenstein, X.; Belle, M.; Domart, M. C.; Larijani, B.; Collinson, L.; Raposo, G.; Salamero, J. *Nat. Methods* **2017,** 14, (2), 102-103.